https://doi.org/10.5194/egusphere-2023-1585
Preprint. Discussion started: 17 July 2023

Paleoearthquake reconstruction on an impure limestone fault scarp at Sparta, Greece

Bradley W. Goodfellow[1,2,3,4], Marc W. Caffee[5,6], Greg Chmiel[5], Ruben Fritzon[1,3#], Alasdair Skelton[2,3], Arjen P. Stroeven[1,3*]

[1]Geomorphology and Glaciology, Department of Physical Geography, Stockholm University, Stockholm, Sweden
[2]Department of Geological Sciences, Stockholm University, Stockholm, Sweden
[3]Bolin Centre for Climate Research, Stockholm University, Stockholm, Sweden
[4]Geological Survey of Sweden, Killiansgatan 10, Lund, Sweden
[5]Department of Physics and Astronomy/Purdue Rare Isotope Measurement Laboratory, Purdue University, West Lafayette, USA
[6]Department of Earth, Atmospheric, and Planetary Sciences, Purdue University, West Lafayette, USA

*Corresponding author
Email: arjen.stroeven@natgeo.su.se
Phone: +46(0)8-16 4230
[#]Now at Celsiusskolan, Sporthallsvägen 7, 828 33 Edsbyn, Sweden

Abstract

Reliable reconstructions of paleoseismicity are useful for understanding, and mitigating, seismic hazard risks. In this study, we apply cosmogenic ^{36}Cl exposure-age dating and concentrations of rare-earth elements and yttrium (REY) to unravelling the paleoseismic history of the Sparta fault, Greece, which is a range-bounding normal fault developed in limestone. Modeling of ^{36}Cl concentrations along two vertical profiles on the Sparta Fault indicates a clustering of four earthquakes within a 1.5 kyr period that culminated with the 464 B.C.E. event that devastated Spartan society. Cumulative uplift was as high as 2.8 mm yr^{-1} during that period, compared with ~0.6–0.9 mm a-1 over the preceding 2.7–4.4 kyr. Because earthquake activity may shift between faults in extensional settings, a large magnitude earthquake is not necessarily indicated as being overdue by the present ~2.5 kyr quiescent period. More generally, accurate identification of individual earthquakes is presently constrained by spatial variations in ^{36}Cl concentration profiles that reflect neither exposure duration nor imprints of former soil profiles. In cases where this is attributable to

mineralogical variations, such as in the Sparta fault scarp, present chemical preparation techniques for AMS measurement of ^{36}Cl may insufficiently account for those variations.

The Sparta fault scarp is composed of fault breccia, which contains quartz and clay-lined pores, in addition to host rock-derived clasts of calcite and microcrystalline calcite cement. The exchange of REY between the hanging wall colluvium and the fault scarp calcite, which has been applied to the study of paleoseismicity on other limestone normal faults, is overwhelmed on this fault scarp by REY attached to the breccia pore clays. Holocene earthquakes and their magnitudes, inferred from fault slip lengths, therefore cannot be inferred from REY data for impure limestone faults such as the Sparta fault but, rather, these data may indicate processes of fault evolution in the Earth's near surface.

Keywords

^{36}Cl exposure dating; earthquake; limestone; normal fault; REY elements; Sparta fault

1 Introduction

Seismic hazard risks are significant in many parts of the world and studying the magnitude, recurrence, mechanisms, and impacts of past earthquakes helps form a basis for mitigating current and future risk. While historical earthquake records are a crucial archive (Gürpinar, 2005), their spatial distribution is patchy and the recurrence interval of large earthquakes on many faults exceeds historical record lengths. Paleoseismic studies that use geologic evidence to infer past earthquakes, and even potentially unravel key earthquake characteristics, such as timing, recurrence intervals, and the magnitudes of slip and shaking intensity, are therefore an

https://doi.org/10.5194/egusphere-2023-1585
Preprint. Discussion started: 17 July 2023

essential component of seismic hazard risk mitigation (McCalpin, 2009, p. 24). Topographic expressions of tectonic faults, the displacement of surficial sediments revealed in trenches, and geochemical alterations on subaerially exposed fault surfaces, may each provide evidence useful to the study of paleoseismicity (e.g., Benedetti et al., 2002; Dramis and Blumetti, 2005; Michetti et al., 2005; Carcaillet et al., 2008; Manighetti et al., 2010; Mouslopoulou et al., 2011; Smith et al., 2014; Cowie et al., 2017; Mozafari et al., 2022). In this study we use cosmogenic ^{36}Cl and concentrations of rare-earth elements and yttrium (REY) to study the paleoseismic history of the Sparta fault at Anogia, Greece (Fig. 1a, b).

The Mediterranean is a densely populated seismically active region that was subjected to 7360 earthquakes of magnitude *(M)* > 4 during 1998–2010 (Godey et al., 2013). Within the Aegean tectonic plate (Fig. 1a), and around its margins, there were >1450 such earthquakes during this period, 77 of which were *M* > 5. In central Greece, earthquakes are associated with normal faults, which occur because of extension of the Aegean plate (Jolivet et al., 2013). In limestone, they may be identified by spectacular scarps, which form from the accumulation of bedrock slip that occurs during successive earthquakes. Holocene fault scarps can be well-preserved (Armijo et al., 1991), which makes them potentially suitable targets for paleoseismic studies.

Earthquakes inferred from incremental slips of limestone normal faults have been dated with concentrations of *in situ*-produced cosmogenic ^{36}Cl (Zreda and Noller, 1998; Mitchell et al., 2001; Benedetti et al., 2002; Palumbo et al., 2004; Schlagenhauf et al., 2010; Tesson et al., 2016; Cowie et al., 2017; Mozafari et al., 2022). This nuclide is produced from spallogenic and muonic reactions that occur in ^{40}Ca when limestone is exposed to cosmogenic radiation. Following an earthquake, the newly exposed scarp segment accumulates ^{36}Cl, the

https://doi.org/10.5194/egusphere-2023-1585
Preprint. Discussion started: 17 July 2023

concentration of which is dependent upon the duration of subaerial exposure, thereby potentially allowing the earthquake to be dated. More recently, ^{36}Cl dating has been complemented with measurements of REY because their distribution vertically along fault scarps may indicate imprints of former hanging-wall soil REY that have been uplifted by successive earthquakes (Carcaillet et al., 2008; Manighetti et al., 2010; Mouslopoulou et al., 2011; Moraetis et al., 2015). Peaks in REY may represent former soil surfaces and their spacing may permit paleoseismic inferences such as the number of slip events, vertical displacement lengths, and earthquake magnitudes. These inferences can be made independently of ^{36}Cl measurements, which can help to verify and strengthen interpretations of past earthquakes using this nuclide.

A pioneering cosmogenic ^{36}Cl study of the Sparta fault by Benedetti et al. (2002) guided our interest because they found evidence at Parori (Fig. 1b) for the historically recorded 464 B.C.E. earthquake that destroyed Sparta (Armijo et al., 1991), and inferred an additional five older earthquakes. However, they were unable to date the historical slip at nearby Anogia. Our study objectives were to: (i) Re-date the paleoseismicity of the Sparta fault at Anogia, to test for the surprising absence of the 464 B.C.E. earthquake, by taking advantage of recent advances in both the measurement of ^{36}Cl and earthquake modelling that accounts for all ^{36}Cl production pathways and shielding effects (Schlagenhauf et al., 2010), and; (ii) Complement the ^{36}Cl dating with measurement of REY to best constrain the paleoseismic history of this fault.

2 Geological Setting

https://doi.org/10.5194/egusphere-2023-1585
Preprint. Discussion started: 17 July 2023

The Sparta fault is a 64 km long, NNW–SSE striking, range-bounding normal fault in southern Peloponnese (Fig. 1a, b). It separates the eastern flank of the Taygetos Mountains (maximum elevation of 2407 m a.s.l.) from the Sparta Basin (Fig. 1b). The Sparta fault is part of a larger normal fault system, which exceeds 150 km in length, and is matched on the western margin of the Taygetos Mountains by the antithetical Kalamata fault and other similar faults located offshore of the Mani Peninsula (Fig. 1a; Armijo et al., 1991). The subaerially exposed scarp of the Sparta fault is developed in late Senonian-Eocene limestones of the Ionian unit (Institute for Geology and Subsurface Research, 1969; Armijo et al., 1991). Folded and tilted Permian to early Triassic pelitic and psammitic sedimentary and metasedimentary units outcrop in the Taygetos Mountains and are also offset by the Sparta fault at depth (Institute for Geology and Subsurface Research, 1969; Armijo et al., 1991). Geomorphic evidence for Quaternary uplift along the eastern flank of the Taygetos Mountains includes steep triangular facets (20°–40°) that are hundreds of meters high along the central portion of the range and decrease in height towards the N and S, wineglass canyons, perched valleys, and alluvial fans having up to 4 m of entrenchment near the Sparta fault trace (Armijo et al., 1991; Benedetti et al., 2002; Pope and Wilkinson, 2005; Papanikolaou et al., 2013). Collectively, the evidence indicates a tectonically active environment.

The Sparta fault scarp is nearly continuous along strike and it reaches a maximum height of 10–12 m in its central portion but tapers towards both ends. Hanging wall erosion associated with stream incision can locally form higher scarp segments. The scarp has a 65°–68° dip and, in all but a few locations, slickensides have been eroded away following exhumation. The slope of the hanging wall ground surface matches that upslope of the footwall, which indicates a contiguous hillslope prior to formation of the present scarp and that sediment accumulation at the scarp base is generally minor. However, wedges of sediment are locally present on the hanging wall and in some places are welded to the scarp face, in positions now perched above the hanging wall (Fig. S1). These wedges may have been perched by earthquake-induced displacement on the Sparta fault or are debris deposits from mass movements that have partly eroded. It is possible that other sediment wedges were also formerly attached to the scarp face but have since fallen off.

Our sampling site is located at Anogia, where the Sparta fault scarp is 6.8 m high (Fig. 1c), sparsely fractured, and displays a smooth surface texture (Fig. 1d-e). Slickenside traces are visible, and the surface displays a black coating, like those commonly occurring on limestone and which contain higher concentrations of SiO_2 and Al_2O_3 than the underlying rock (Carcaillet et al., 2008). The scarp surface at Anogia also displays a spatially variable distribution of subaerial weathering features such as rills and dissolution pits, which we avoided in our sampling. The lower-angle hillslopes on both the foot wall (above the fault scarp) and hanging wall display a patchy distribution of frequent bedrock outcrops and an indurated allochthonous regolith composed of limestone clasts, with a matrix of red aeolian dust and calcite cement. An outcrop of limestone about 50 m upslope of the fault scarp reveals folded and tilted bedding. The bedding nearest to the scarp has a dip of 45–60° and a strike of 268–279°, which corresponds with those for the fault scarp, indicating that faulting appears to exploit these structural weaknesses in the bedrock.

3 Methods

https://doi.org/10.5194/egusphere-2023-1585
Preprint. Discussion started: 17 July 2023

To study the paleoseismicity of the Sparta fault, we combined Accelerated Mass Spectrometry (AMS) measurements of cosmogenic ^{36}Cl concentrations from samples collected from the Sparta fault scarp with field and laboratory analyses of scarp composition and mineralogy, and with field measurements of hanging wall soil composition and pH. We made these measurements by sampling a vertical ^{36}Cl profile at Anogia, upwards from the ground surface and adjacent to the sampling transect of Benedetti et al. (2002) for direct comparison with that pre-existing record (Fig. 1c). We also took samples for ^{36}Cl and mineralogical analyses, including REY, from a second vertical profile located about 50 m to the south (Fig. 1c). We chose this additional site for its smooth, non-fractured, fault scarp surface, and sampling was completed from the top of the scarp to 80 cm below the present ground surface, following hand excavation of a pit.

3.1 ^{36}Cl concentrations

We sampled the first profile, adjacent to the southern margin of the Benedetti et al. (2002) profile, for ^{36}Cl by using an angle grinder to cut 10*20*2.5 cm (*h**w*d*) slabs from the ground surface to a height of 3.9 m (Fig. 1c, d). Because of a crack in the fault scarp at 1.1 m above the ground, the transect was shifted sideways (towards the north) by 40 cm, thus duplicating the measurement at 1.1 m. A total of 37 samples from this profile were measured for ^{36}Cl concentration. We sampled the second profile, ~ 50 m further to the south, for ^{36}Cl and mineralogical analyses initially by drilling 14 cores of 4 cm diameter to a depth of 3 cm into the scarp surface (Fig. 1c, e). Four of these cores were spaced at 20 cm intervals below the ground surface and eight were spaced at 80 cm intervals above the ground surface to a height of 6.4 m, which is 0.4 m below the top of the scarp. These samples were augmented by another two drill core samples at 1.2 m and at 6.0 m. Subsequently, we took 20 samples from this profile using an angle grinder to cut 10*20*2.5 cm (*h**w*d*) slabs from the ground

https://doi.org/10.5194/egusphere-2023-1585
Preprint. Discussion started: 17 July 2023

surface to a height of 2.0 m (Fig. 1c). A total of 71 samples from the three profiles were subjected to preparation chemistry for ^{36}Cl targets and measured using AMS.

For ^{36}Cl measurements, limestone samples were crushed to approximately 0.5 mm diameter and the whole sample was used without removing any size fraction through sieving. Prior to partial dissolution approximately 120 g of crushed material was washed with deionized water to remove fines. Following Stone et al. (1996), meteoric ^{36}Cl was removed using two cycles of partial dissolution with nitric acid to dissolve 5% (by mass) of the carbonate each time. To prepare the AMS target we used 30 g of dried sample, spiked with 1 mg of ^{35}Cl-enriched sodium chloride carrier (Source: Icon Isotopes, ^{35}Cl 99.635 atom %, $^{35}Cl/^{37}Cl = 273$) to measure native chloride by isotope dilution. A slurry of the sample and 120 g of deionized water was slowly dissolved with 60 g of concentrated trace-metal grade nitric acid. Post-dissolution, both liquid and undissolved solids were quantitatively transferred to a centrifuge bottle where the solids were removed by centrifugation. The supernatant was decanted to another centrifuge bottle and chloride was precipitated using one molar silver nitrate. After a settling period, the bottle was centrifuged to isolate the silver chloride which was then washed, dissolved with ammonium hydroxide, and treated with barium nitrate to remove sulfate in preparation for further purification by chromatography. The solution was loaded onto 5 ml of Bio-Rad AG 1-X8 strong anion-exchange resin and chloride was moved through with 0.50 mmol, and then 0.150 mmol, nitric acid. After re-precipitation with silver nitrate and a washing step the silver chloride was dried and packed into silver bromide-cored copper holders. AMS measurements were performed at the Purdue Rare Isotope Measurement Laboratory according to procedures in Muzikar et al. (2003); standards used for the measurement are described in Sharma et al. (1990).

https://doi.org/10.5194/egusphere-2023-1585
Preprint. Discussion started: 17 July 2023

We applied a model developed by Schlagenhauf et al. (2010) for the interpretation of earthquakes from cosmogenic ^{36}Cl concentrations to the Sparta fault scarp. This model accounts for various parameters that control the ^{36}Cl concentration in a limestone normal fault scarp, including geomagnetic field variations, host rock and hanging wall colluvium chemical compositions and densities, scarp erosion rate, shielding of the scarp base by a colluvial wedge, and the geometries of the fault scarp, the slope above the scarp, and the hanging wall colluvial wedge. Their model uses three statistical parameters, the weighted root mean square (RMSw), the reduced Chi-square (χ^2_{red}), and Akaike Information Criterion (AIC) to assess the quality of fit between modelled and measured data to provide an objective assessment of the number, and spatial and temporal spacing, of inferred earthquakes. For our age calculations, we used the sea-level high-latitude (SLHL) ^{36}Cl production rate from spallation in calcite of 59.4 atoms g^{-1} yr^{-1} and a temporally variable geomagnetic field to scale the ^{36}Cl production rate from Lifton et al. (2005). A more recent ^{36}Cl production rate calibration by Marrero et al. (2016) is not used here because it is scaled using Lifton et al. (2014), which is not included in the model of Schlagenhauf et al. (2010). The Marrero et al. (2016) production rate overlaps with the ^{36}Cl production rate from Lifton et al. (2005), within uncertainty. We complemented the modelling of our new ^{36}Cl results with a re-modelling of the Benedetti et al. (2002) data, using our own data for fault scarp and colluvium composition. Our method of inferring earthquakes was based on fitting ^{36}Cl concentration profiles derived from the Schlagenhauf et al. (2010) model to the actual ^{36}Cl concentration profiles and inferring former soils surfaces from inflection points in the real ^{36}Cl concentration profiles. This allows us to best constrain the paleoseismic history of the Sparta fault over the late Holocene.

3.2 Sparta fault scarp composition

Fault scarp chemical composition and mineralogy were analyzed from the second sampling profile, 50 m to the south of the first sampling profile, as follows. An initial elemental analysis was done in the field on the Sparta fault scarp surface using an Olympus Innov-X Delta (40 kV) handheld X-ray fluorescence (XRF) device. This instrument performs elemental analyses with a circular sample spot of 8 mm diameter and can measure elements heavier than Na. All elements lighter than Mg are reported as lighter elements (LE). Of the elements that compose REY, it was only capable of measuring yttrium. Sampling was done at an interval of 5 cm (or less) over a 7.7 m vertical profile, beginning ~90 cm below the hanging wall soil surface. This profile corresponds with the location of the drill core and 2.0 m-long ^{36}Cl profiles but was measured before either drilling or slab sampling (Fig. 1c).

For more detailed analyses of elements, including REY, a total of 39 cores (22 mm and 35 mm diameters and to depths of ~4 cm) were collected every 20 cm from the fault scarp vertical transect using a portable drill (Fig. 1d). The outermost 1 mm was removed from each core prior to crushing to avoid contamination from the black surface coating. The next 15 mm of each core were then rinsed with cold water, air dried, and crushed using a grinder with a steel mortar to a grain size of <100 µm. This crushing technique might supply additional REY to samples (Hickson and Juras, 1986) but if so, this likely occurs systematically across samples and we are more interested in spatial trends, which we confirm independently using the handheld XRF, than absolute abundances. The crushed samples were then analyzed for major and trace elements using fusion inductively coupled plasma mass spectrometry (FUS-ICP-MS) at Activation Laboratories (Ontario, Canada).

We complemented the FUS-ICP-MS analyses with spot elemental analysis of one rock core from 1.1 m above the scarp base to make a high-resolution determination of any spatial

https://doi.org/10.5194/egusphere-2023-1585
Preprint. Discussion started: 17 July 2023

variations in the scarp composition. This was done with an energy-dispersive X-ray spectroscope (EDS) attached to an environmental scanning electron microscope (ESEM). We used a Quanta FEG 650 with Oxford-Inka EDS, and the analysis was made in a high-vacuum environment at 20 kV. The technique is incapable of detecting REY because their concentrations are too low. Photomicrographs and backscatter images of pore spaces were also taken using the ESEM. These analyses were completed at the Department of Geological Sciences, Stockholm University.

3.3 Sparta fault scarp mineralogy

A modal analysis of mineral fractions was completed on thin sections taken from the remaining 38 core samples. This was done by counting 1000 points on each thin section (Hutchison, 1974) using a Pelcon automatic point counter, attached to a Leica (DM LSP) optical microscope. This point counter comprises a stepping frame attached to a control box (power supply) and is also connected to a computer for statistical analyses using Pelcon software version 2. The point counting and mineral identification was made using an objective working distance of 1.52 mm. The line section pre-set step-length was 0.3 mm and the line section distance was 1.5–2 mm. The point counting permitted a detailed quantitative analysis of the mineralogy of the Sparta fault scarp surface. This detailed mineralogy was then compared with the chemical composition data to determine whether phases other than the host limestone are present.

3.4 Hanging wall soil chemistry and pH

Soil chemistry and pH were measured in samples taken at ~10 cm intervals to a depth of ~90 cm in the pit excavated at the base of the Sparta fault scarp (Fig. 1c). The elemental analysis was again done with the handheld XRF device. Indicator strips were used to measure pH from mixtures of 1:1 mass ratio of soil:distilled water, and soil:1 M KCl (Sikora and Moore, 2014). These analyses help determine the vertical distribution of REY in the soil (using yttrium as a proxy) and indicate how they might correlate with pH and the vertical distribution of REY in the fault scarp below the soil surface.

4 Results

4.1 Sparta fault ^{36}Cl concentrations

The cosmogenic nuclide ^{36}Cl concentrations from our three profiles (Table S1) and the original Benedetti et al. (2002) ^{36}Cl concentrations are compared in Figure 2. The lowest ^{36}Cl concentrations occur in our drill-core samples. Whereas age reversals are non-apparent in this profile, comprised of widely dispersed sample points, there is a clear decrease in ^{36}Cl with depth, including below the soil surface. Our 2.0 m- and 3.9 m-long profiles display corresponding trends with increasing concentrations with increasing height on the fault scarp. Only at 1.6 m do the trends strongly deviate from each other. The 2.0 m-long profile indicates generally lower ^{36}Cl concentrations including six of 19 points that do not overlap within uncertainty of data points at corresponding elevations on the 3.9 m-long profile. Four of those points are located from 1.0 m to 1.3 m. In comparison with our 3.9 m-long profile, the adjacent segment of the Benedetti et al. (2002) profile shows ^{36}Cl concentrations that are on average 19% higher (0-4 m). Uncertainties (1σ) for data points comprising each profile are almost identical, displaying a mean of 3.8% for the Benedetti et al. (2002) profile versus 3.9% for our 3.9 m-long and 2.0 m-long profiles. However, the Benedetti et al. (2002) profile displays more variation between adjacent sample points than is evident in our profiles. Whereas concentrations differ between the three longest profiles, they show a consistent gradient up to ~4 m on the scarp face equivalent to an average uplift rate of 1.0–1.3 mm yr^{-1}.

https://doi.org/10.5194/egusphere-2023-1585
Preprint. Discussion started: 17 July 2023

Above 4 m on the scarp, both our drill-core profile and the Benedetti et al. (2002) profile display matching lower gradients, which indicates a lower average uplift rate of 0.6–0.9 mm yr^{-1}. If uplift rates are alternatively calculated as occurring prior to the subaerial exposure of the lowermost samples by the most recent earthquake, cumulative uplift rates increase to 2.8 mm yr^{-1} and 1.8 mm yr^{-1} for the lower parts of the 3.9 m-long and Benedetti et al. (2002) profiles, respectively. Both our 2.0 m-long and 3.9 m-long profiles indicate a local low in ^{36}Cl concentration at ~0.5 m above the ground surface, which is opposite to the Benedetti et al. (2002) profile, where concentrations reach a local high at ~0.5 m. Both of our profiles also display an age reversal at 1.4–1.6 m, which is comparable to the age reversal at 1.2–1.5 m on the Benedetti et al. (2002) profile. Our 3.9 m-long profile and the Benedetti et al. (2002) profile each display additional age reversals at 2.6–2.7 m and 3.1–3.2 m on the scarp. Another reversal is also apparent at 3.7–3.9 m in both profiles (including the drill-core sample at 4 m). These reversals complement the gradients in being similarities shared by the profiles that are key characteristics for a further analysis of its paleoseismicity using the model of Schlagenhauf et al. (2010).

Using the Schlagenhauf et al. (2010) model, we analyze the number, ages, and magnitudes of earthquakes inferred from a composite ^{36}Cl concentration profile; principally this record contains the 3.9 m profile, but also includes the subsurface samples from our drill-core profile, and the drill-core samples from 4.1 to 6.4 m (Fig. 3a). The total length of this record then becomes 7.2 m. To match these two data sets, we increase the concentration of each drill core sample by 5%. Integrating these two data sets is necessary to generating fits to the ^{36}Cl data because subsurface data are required by the Schlagenhauf et al. (2010) model. The 5% is chosen to match the ^{36}Cl concentrations in the four drill core samples between 0.8 m and 2.4 m with those in the corresponding segments of the 2.0 m and 3.9 m profiles, while maintaining subsurface ^{36}Cl concentrations below those in the samples at 0.1 m on the 2.0 m and 3.9 m profiles. Then, using the same parameters that generated the best model fit to the 3.9 m-long plus drill-core profile (Table 1), we apply the best model fit to our 2.0 m-long profile (Fig. 3b) and the Benedetti et al. (2002) profile (Fig. 3c). In both cases, we use the adjusted subsurface data from the drill-core profile. For our 2.0 m plus subsurface drill core profile, we used the scarp mineralogy measured for each sample. For the 3.9 m-long plus drill core profile and the Benedetti et al. (2002) plus subsurface drill core profile we used a mean composition from our measured scarp mineralogy because we did not determine mineralogies along these profiles. We further compare earthquakes modelled from age reversals in the ^{36}Cl data with earthquakes modelled from potential soil profiles mirrored in scarp geochemistry (REY, SiO_2 and Al_2O_3; Fig. 3d). We then use all data to infer the most likely earthquake history for this segment of the Sparta fault.

From the combined 7.2 m-long profile, modelling indicates that five earthquakes at 1.4 m (2.3 kyr B.P.), 2.6 m (2.8 kyr B.P.), 3.9 m (3.2 kyr B.P.), 5.1 m (3.8 kyr B.P.), and 6.5 m (5.9 kyr B.P.) provide the best statistical fit to our data (Fig. 3a; Table 1). Our best fit parameters, taken either directly from field measurement or assumed (in the case of ε and pre-exposure), are listed in Table 1. The two inferred earthquakes at 1.4 m (2.3 kyr B.P.) and 2.6 m (2.8 kyr B.P.) also provide a good statistical fit to our 2.0 m-long profile (Fig. 3b). An inferred five earthquakes on the Benedetti et al. (2002) profile (Fig. 3c) at the same elevations on the scarp as our adjacent composite profile (Fig. 3a) display a statistically weaker fit than obtained for our data (Table 1). Older ages and longer exposure prior to the oldest earthquake (pre-exposure) are necessitated by the systematically higher ^{36}Cl concentrations. Earthquakes inferred from the record of scarp geochemistry (Section 4.3) occur at 0.8 m (1.9 kyr B.P.), 2.6 m (2.8 kyr B.P.), 4.0 m (3.0 kyr B.P.), and at 6.4 m (5.9 kyr B.P.) on our 7.2 m-long profile

(Fig. 3d). Interestingly, this reconstruction has a statistically weaker fit than for earthquakes inferred from reversals in ^{36}Cl concentrations (Fig. 3a; Table 1). We note that for the applicable ^{36}Cl concentration profiles, model fits overestimate ^{36}Cl concentrations at 4 m on the scarp surface (Figs. 3a, c, and d). In Figure 3a, c, and d, an (artificial) earthquake is added to the top of the ^{36}Cl concentration profile to fit all data (Earthquake 1, shown in grey). Because this oldest earthquake is tied to the highest sample on the scarp, without an associated age reversal, and because ^{36}Cl measurements are sparely spaced above 4 m, the inferred locations on the fault scarp and timing of this earthquake are approximate. We therefore focus our interpretations on the inferred earthquakes lower down on the fault scarp.

The model fit to our data is sensitive to input parameters, at least two of which are difficult to accurately measure (Fig. 4). It is most sensitive to the scarp dip angle (e.g., a 5° decrease causes the AICc to increase by 12%), followed by the density of colluvium mantling the hanging wall and the rate of scarp surface erosion. It is least sensitive to variations in rock density and hillslope gradient. The colluvium density depends on relative abundances of limestone clasts, mineral soil, organic matter, and water, which vary spatially. Due to, for example, wetting and drying, colluvium density is expected to also vary temporally. Scarp erosion rates remain undetermined. The adopted values for colluvium density and scarp erosion rate are, therefore, those which provide the best model fits to the data. In both cases, those values are also realistic (Table 1). Rock density is prescribed from the literature and colluvium dip, scarp dip, and hillslope gradient are based on measurements. Optimal colluvium and scarp dips are adjusted slightly relative to measured values (i.e., 1–2°, which is within measurement uncertainty).

4.2 Granulometry of the Sparta fault scarp surface

https://doi.org/10.5194/egusphere-2023-1585
Preprint. Discussion started: 17 July 2023

A first look at the Sparta fault scarp surface yields a misleading impression of homogeneous limestone (Figs. 1, 5a), whereas close inspection of the core samples instead reveals a typical fault breccia (Figs. 5b-d). This breccia consists of angular-to-rounded limestone clasts with axes of 1–7 mm (in the two-dimensional view provided by thin sections) surrounded by matrix/cement in which clasts are <0.1 mm in length. The fault breccia is defined as a protocataclasite, according to the classification of Woodcock and Mort (2008). The composition of the protocataclasite displays large spatial variations, with some portions containing abundant clasts (Fig. 5c), whereas others are dominated by fine matrix (Fig. 5d). The proportion of clasts >2 mm ranges from 5% to 20% vertically along the fault scarp and the proportion of matrix ranges from 5% to 60%. We did not measure the thickness of the protocataclasite but it everywhere exceeds the 4 cm depth of our drill cores.

4.3 Sparta fault scarp composition and mineralogy

In addition to a spatially variable granulometry, the fault scarp shows a spatially variable distribution of major and trace elements. The major component is, as expected for limestone, CaO (mean 52.22%) but its concentration varies between 43.83% and 56.64% (Table S2), which exceeds spatial variations in CaO seen elsewhere in limestone normal fault scarps (Carcaillet et al., 2008; Tesson et al., 2016). Quartz (SiO_2) also occurs, and it too displays spatial variations (0.10%–20.82%), with broad peaks occurring at -0.5– -0.4 m, 0.9–1.2 m, 4.6–4.8 m, and 6.0–6.2 m along the vertical fault scarp profile (Fig. 6; Table S2). An additional peak in SiO_2, but which is not seen in point counting of quartz, occurs at 6.2 m (Fig. 6; Tables S2 and S3). Mean concentrations of other major elements are low in bulk samples, including Al_2O_3 (0.21%), MgO (0.16%), Fe_2O_3 (0.09%), P_2O_5 (0.07%), and K_2O (0.05%; Table S2). However, EDS measurements, such as shown in Figure 7a, reveal that the concentrations of some elements are frequently much higher in intergranular pores (Fig. 7c)

https://doi.org/10.5194/egusphere-2023-1585
Preprint. Discussion started: 17 July 2023

than elsewhere in the fault scarp, including Si ≤ 38.3%, Al ≤ 11.7%, Fe ≤ 48.4%, and K ≤ 7.1% (Table S4). Furthermore, intergranular pores and quartz frequently occur together (Fig. 7b) and the concentration of Al_2O_3 covaries with the much more abundant quartz (SiO_2) (Fig. 6).

Quartz is revealed by microscopy to be present as randomly oriented rounded-to-angular grains that are <50 µm in diameter (Figs. 5d, 7b). Quartz is a constituent of the protocataclasite fine matrix that is mostly comprised of microcrystalline calcite precipitates and which cements larger host rock-derived $CaCO_3$ clasts (Figs. 5b-d, 7b, 8a). Point counting further reveals quartz modes ranging from 0.1% to 15.4% of thin section area (Table S3), with higher abundances correlating to higher abundances of fine matrix. The spatial correlations between SiO_2, quartz abundances on point counting, and fine matrix are further indicated by the EDS spot elemental analysis (Fig. 8). Here, the two selected spots in the fine matrix display Si abundances of 29.7% and 28.9%, which contrasts with 1.7% and 0.9% for the two spots located on clasts. CaO abundances display an inverse relationship with SiO_2 (33.7% and 31.2% for the clasts versus 4.8% and 5.1% for the fine matrix). SiO_2 is present largely as quartz, as evidenced by the strong spatial correlation between quartz and SiO_2 along the vertical profile (Fig. 6). Quartz can therefore be used as a proxy for fine matrix abundances in the Sparta fault scarp.

In addition to the spatial relationship between quartz and fine matrix, we observed in backscatter SEM images that pore spaces, which frequently harbor higher concentrations of Si, Al, K and/or Fe than host rock-derived clasts, are also more abundant in the fine matrix (Fig. 7c). These observations provide evidence that clay particles (< µm-scale) frequently

https://doi.org/10.5194/egusphere-2023-1585
Preprint. Discussion started: 17 July 2023

coat pore spaces. The abundance of quartz therefore also provides a proxy for the abundance of clay-coated pore spaces.

Concentrations of yttrium are generally low (1.2–11.1 ppm; Table S5) but vary in a wave-like pattern along the vertical profile, with maxima occurring at -0.4 m, 0.8 m, 2.6 m, 4.0 m, and 6.4 m (Fig. 9). These maxima do not systematically decrease with vertical distance above the hanging wall and are not highest in the soil-mantled portion of the scarp. Yttrium (mean 6.3 ppm), La (mean 5.04 ppm), Nd (mean 3.54 ppm), and Ce (mean 2.31 ppm) have the highest concentrations, whereas all other REY are <1 ppm (Table S5). The concentrations of REY elements co-vary vertically along the scarp surface (R^2 = 0.95; Fig. 9), the proportion of light-REY (LREY) to heavy-REY (HREY) remains constant (ratio ~7:1; Fig. 10; Table S5), and concentration maxima occur at locations that correspond closely with the Al_2O_3 maxima (Fig. 9; Table S5). Accordingly, there is a strong correlation between REY and Al_2O_3 (R^2 = 0.92; Fig. S2a). Spatial correlations between REY and SiO_2 and K_2O are also observed (R^2 = 0.56 and 0.87, respectively; Fig. S2c, e). In contrast, the locations of REY maxima correlate neither with the location of the present ground surface (-0.4 m) nor former ground surfaces at 1.4 m and 5.1 m inferred from ^{36}Cl data. There are, however, correlations between REY maxima and former ground surfaces at 2.6 m, 3.9–4.0 m, and at 6.4–6.5 m modelled from the ^{36}Cl data. No systematic relationship is therefore apparent between REY maxima and either the present soil surface or former soil surfaces inferred from inflection points in ^{36}Cl concentrations.

4.4 Hanging wall soil chemistry and pH

The terra rosa soil mantling the hanging wall primarily comprises aeolian dust (Muhs et al., 2010) and carbonate clasts. At our sample site, the soil thickness at the base of the Sparta fault scarp is 0.8 m and this appears to be stable, at least over the timescale of scarp surface dissolution, as evidenced by a much smoother scarp surface texture below the soil surface compared with the subaerially exposed scarp. Below the organic horizon (~0.1 m thick) the soil is welded, probably by calcite precipitates, and horizons are absent. Soil pH is, in general, slightly acidic along the excavated vertical profile, remaining within a 6.2 to 7.0 range (Fig. 11a; Table S6). An outlier occurs at -0.30 m, where the pH is 5.6 ± 0.2. Soil composition varies with depth (Fig. 11b; Table S7). Concentrations of Si, Al, and K are lower in the organic horizon (11%, 0–5%, and 0.4%, respectively) compared with the remainder of the profile (18%–30%, 5–10%, and 0.5–0.9%, respectively), whereas the concentrations of LE, which includes C, are, as expected, higher in the organic horizon (75%–80%) than in the lower profile segment (51%–64%). The concentration of yttrium ranges from a maximum of 36–39 ppm at -0.5– -0.6 m depth to a minimum of 11 ppm at -0.1 m depth and its vertical distribution correlates positively with Si (R^2 = 0.71), Al (R^2 = 0.45), and K (R^2 = 0.54), but negatively with pH (R^2 = -0.52; Figs. 11c, S1b,d,f; Table S7).

5 Discussion

5.1. Modelling of earthquakes from ^{36}Cl concentration profiles

Our modelling using Schlagenhauf et al. (2010) indicates that five earthquakes provide a best fit to the Sparta fault ^{36}Cl data. The youngest inferred earthquake (2.3 kyr B.P.) corresponds both with the historical 464 B.C.E. event and inflections in the ^{36}Cl data of the 2.0 m-long and 3.9 m-long profiles. The penultimate inferred earthquake at 2.8 kyr B.P. correlates to an inflection in ^{36}Cl concentration at 2.6 m in our 3.9 m-long profile. Because data density decreases above 4.0 m, there are no clear inflections in ^{36}Cl concentrations to base the occurrence of earthquakes on for this segment of the scarp. However, fitting the

https://doi.org/10.5194/egusphere-2023-1585
Preprint. Discussion started: 17 July 2023

Schlagenhauf et al. (2010) model to the measured gradient in ^{36}Cl concentrations yields an additional record of three older earthquakes at 3.2 kyr B.P., 3.8 kyr B.P., and 5.9 kyr B.P. to explain the exhumation of the exposed scarp surface. The four most recent earthquakes are clustered within a 1.5 kyr period, whereas nearly 2.5 kyr have elapsed since the last earthquake on the Sparta fault. A lower gradient in ^{36}Cl concentration on the fault scarp above the location of the inferred 3.2 kyr B.P earthquake also indicates a lower rate of scarp exhumation prior to the 1.5 kyr period of apparently higher earthquake activity. The long recent quiescent interval therefore does not necessarily provide evidence that another (large magnitude) earthquake may be imminent. As a comparison, extensional faults in the central Italian Apennines accumulate meters of displacement over several thousands of years, but also display similar length periods where cumulative slip magnitudes are much lower, because earthquake activity shifts between faults across-strike (Cowie et al., 2017). The same may also apply to the Sparta fault and related extensional faults in the region.

The precision at which we can interpret paleoseismicity is constrained by three factors. These include (i) sparse ^{36}Cl data above 4.0 m on the Sparta fault scarp, (ii) uncertainties in scarp erosion rate, pre-exposure length, and hanging wall surface dip angle and colluvium density (Fig. 4), and (iii) fault scarp impurities that produce noise in the ^{36}Cl data and distortion of potential REY indicators of former soil surfaces. Below, we will explore methodological and geological sources of uncertainty in the ^{36}Cl data, reasons for mineralogical impurities in the Sparta fault scarp, and how the observed REY distribution can be interpreted. This will be achieved by comparing the 2.0 m-long profile with the equivalent segment of the 3.9 m-long profile because both profiles have been sampled, processed, and analyzed in the same manner and at the same time, and therefore provide a measure of repeatability.

https://doi.org/10.5194/egusphere-2023-1585
Preprint. Discussion started: 17 July 2023

5.2 Methodological and geological sources of uncertainty in the ^{36}Cl data

A peculiar feature of the ^{36}Cl data is that the profile comprised of small drill-core samples generally yields younger exposure ages for the Sparta fault scarp than the 2.0 m- and 3.9 m-long profiles, which, in turn, are systematically younger than the Benedetti et al. (2002) profile (Fig. 2). The Benedetti et al. (2002) profile displays variations between adjacent sample points that exceed those observed in our profiles and rival variations in ^{36}Cl concentrations that may be attributable to earthquakes. We interpret the systematic differences in ^{36}Cl concentration between the drill-core profile, the 2.0 m and 3.9 m profiles, and the Benedetti et al. (2002) profile as reflecting methodological differences related to advances in sample preparation chemistry at PRIME-Lab, Purdue University. Similarly, the reason why we can directly infer the 464 B.C.E earthquake at Anogia, in contrast to Benedetti et al. (2002), is attributable to advances in age calculations from ^{36}Cl concentrations.

Whereas our 2.0 m- and 3.9 m-long profiles display corresponding trends with increasing elevation on the fault scarp, the 2.0 m profile has generally lower ^{36}Cl concentrations (Fig. 2). Indeed, six of its 19 ^{36}Cl concentrations do not overlap within uncertainty with concentrations of corresponding samples on the 3.9 m profile, including four points located between 1.0 m and 1.3 m. We interpret these differences as indicating that the fault scarp of the 2.0 m profile has been either partly shielded from cosmogenic radiation, has eroded more than the surface of the 3.9 m profile, or contains a higher concentration of impurities. Of potential additional relevance is that the texture of the scarp surface at the location of the 2.0 m profile is smoother than at the location of the 3.9 m profile. Because a similarly smooth texture also characterizes the scarp surface presently buried by colluvium mantling the hanging wall, the smooth texture at the location of the 2.0 m profile may indicate either recent burial of the scarp surface by colluvium and/or $CaCO_3$ dissolution occurring at a higher rate than at

https://doi.org/10.5194/egusphere-2023-1585
Preprint. Discussion started: 17 July 2023

locations where the exposed scarp surface texture is rougher. If a smooth texture reflects erosion through $CaCO_3$ dissolution, there might be preferential flow, or seepage, of water from the hillslope above the scarp at the location of the 2.0 m profile. Observed lumps of colluvium cemented to the Sparta fault scarp, at locations perched above the present hanging wall surface (Fig. S1) partially shield the underlying scarp surface. However, had this previously occurred at the location of our 2.0 m profile, an eroded colluvial lump would be evidenced in the hanging wall sediments. On the contrary, there is no colluvial lump, but rather a sub-horizontal surface is present with an expression that differs little from the surface below the 3.9 m profile. The inter-profile differences in ^{36}Cl concentrations illustrate the value in taking samples for ^{36}Cl measurements from more than one vertical profile, because evidence of past shielding by sediments or bedrock can otherwise be difficult, at best, to detect. Partial shielding may impact the interpretation of the number of paleoearthquakes and result in lower age estimates of earthquakes, with a corresponding decrease in recurrence intervals.

5.3. The effects of mineralogical impurities on ^{36}Cl concentration profiles

Mineralogical impurities embedded in the fault breccia that comprises the scarp surface appear to be a key geological reason for spatial variations in the concentration of ^{36}Cl. This effect is best evidenced when comparing modelled ^{36}Cl concentrations for the 2.0 m-long profile (Fig. 3b), including measured mineralogy for each sample location, with modelled ^{36}Cl concentrations for the 3.9 m-long and Benedetti et al. (2002) profiles, including mean values of the scarp composition derived from our measured data (Fig. 3a, c, d). Whereas the latter modelled profiles appear smooth, the modelled 2.0 m profile contains inter-sample noise, which reflects variations in calcite abundance, attributable to the additional, and variable, presence of quartz and other minerals, including trace amounts of clay lining pores

https://doi.org/10.5194/egusphere-2023-1585
Preprint. Discussion started: 17 July 2023

(Figs. 5–9). Because ^{36}Cl is also produced by spallation on K (162 ± 24 atoms g^{-1} yr^{-1} at SLHL; Evans et al., 1997), Fe (1.9 ± 0.2 atoms g^{-1} yr^{-1} at SLHL; Stone, 2005), and Ti (13 ± 3 atoms g^{-1} yr^{-1} at SLHL; Fink et al., 2000), noise in the ^{36}Cl data might also partly reflect the relative abundances of these elements. However, for the case of the Sparta fault, this appears to be insignificant given that measured concentrations of these elements are extremely low (concentrations of K_2O, Fe_2O_3, and TiO_2 are 0–0.12%, 0.03–0.24%, and 0–0.02%, respectively; Fig. S3, Table S2).

Mineralogical impurities may also explain two other enigmatic features in the ^{36}Cl data. Firstly, an apparent age reversal occurs at 3.1 m in the 3.9 m-long profile (Fig. 3a). Although this could indicate the location of a former soil horizon and thus inferred displacement by an earthquake, a better model fit is gained by locating an earthquake higher up the scarp at 3.9 m. Secondly, ^{36}Cl concentrations at ~4 m in the 3.9 m profile and the Benedetti et al. (2002) data (3.8-4.1 m, Fig. 3a; 3.7-4.3 m, Fig. 3c) are too low to overlap within uncertainty with concentrations modeled using Schlagenhauf et al. (2010). A possible explanation for both enigmatic features is an inability to fully capture the effects of mineralogical impurities on ^{36}Cl production rates. This is largely because, in the absence of mineralogical data for these profiles, we have calculated a mean composition based on the mineralogical data for the 2.0 m profile to model ^{36}Cl concentrations. However, even with the mineralogical data, current laboratory techniques for preparing samples for ^{36}Cl measurement may not record mineralogical variations at sufficient precision. In addition to highlighting the importance of mineralogical analyses, we also highlight the value of using a model to identify the likely displacements by paleoearthquakes through fitting model ^{36}Cl concentration profiles to real ones, rather than overtly relying on apparent age reversals. It remains possible that two earthquakes occurred in close succession, but with this data and methodology, we cannot confidently infer both of those.

5.4. Estimated magnitude of the 464 B.C.E. earthquake

The 464 B.C.E. earthquake that destroyed Sparta had an estimated moment (M_o) of 1 – 4 (x 10^{19}) N m. This is derived from multiplying the vertical displacement of 1.4 m (Fig. 3a-c) with fault dimensions of 20 x 14 km – 64 x 14 km, and with a shear modulus of 3.23 x 10^{10} N m^{-2} (Armijo et al., 1991). The values of 20 km, 14 km, and the shear modulus are from Armijo et al. (1991) and 64 km is the mapped length of the Sparta fault in Figure 1. This estimated range of M_o values straddles a previous "most probable" estimate of moment by Armijo et al. (1991) of 3 x 10^{19} N m even though they lacked field constraints on fault slip distance during the Sparta Earthquake. Hence, we conclude from this congruence of the probable value with values based on the vertical displacement modelled from the ^{36}Cl data (Fig. 3), that they are reliable. From the empirically derived equations of Pavlides and Caputo (2004) and a vertical displacement of 1.4 m of the Sparta fault, we calculate a magnitude (M_s) of 6.8-7.2 for the 464 B.C.E. earthquake. Given the severe destruction inflicted upon the Spartan society (REF?), we consider that the upper estimate is most likely. A magnitude 7.2 earthquake is also in agreement with the estimate by Armijo et al. (1991), although they based this on ~10 m of vertical displacement. We are less certain of the magnitudes and timing of older earthquakes. However, it appears that the Sparta fault was exhumed by a series of similarly large earthquakes over a period of about 3.5 kyr.

5.4. Interpretation of REY distributions

REY cannot be used to infer imprints of former soil profiles on the Sparta fault at Anogia. Petrographic analyses indicate that the Sparta fault scarp is composed of a protocataclasite consisting of calcite clasts derived from the host limestone, microcrystalline calcite cement, and quartz (Figs. 5, 6). Furthermore, EDS analysis indicates that trace amounts of clay, such as illite, are lining pores where microcrystalline calcite cement and quartz are located (Fig. 7; Carcaillet et al., 2008). Given the correlations between REY and each of Al, K, and Si (R^2 = 0.92, 0.87, and 0.56, respectively; Fig. S2a-c), we infer that the clays embedded in the fault scarp are hosting REY. This is a likely explanation for why REY peaks 0.4 m below the current soil surface (Fig. 9), rather than at the soil surface as has been observed on the Magnola fault in Italy (Manighetti et al., 2010).

The formation of protocataclasite occurs beneath the Earth's surface at depths that may range from meters to up to thousands of meters. A model for this involves fluids moving along the Sparta fault, primarily associated with seismic events. These fluids dissolve $CaCO_3$ from the host-limestones and potentially also silicate minerals from psammitic and pelitic (meta)sediments, where they are dissected by the fault. In association with variations in temperature and pressure along the fault, chemical saturation of these fluids results in precipitation of clay, quartz, and microcrystalline calcite, which cements clasts of host-rock derived limestone into the fault breccia. Subsequent faulting re-fractures the breccia and particle comminution over time produces quartz grains that are rounded-to-angular in shape, randomly oriented, and <50 µm (Figs. 5, 7). The fault breccia may also have undergone multiple generations of microcrystalline calcite re-cementing from re-circulating fluids. As an alternative to a dissolution-precipitation model, clay and quartz emplacement may involve fluid entrainment of particles and grains from clay- and quartz-bearing sedimentary units during faulting, as has been observed elsewhere (e.g., Darwin, 1840; Roy, 1946; Brandon, 1972; Röshoff and Cosgrove, 2002). This process may also be accompanied by comminution of fault-zone quartz grains derived from psammitic rocks. We tentatively exclude a

https://doi.org/10.5194/egusphere-2023-1585
Preprint. Discussion started: 17 July 2023

contemporary aeolian source for the clay and quartz because there is no documented mechanism to transport clay particles and quartz grains from the soil to centimeters into a fault scarp. We cannot distinguish soil to scarp clay and quartz migrations on the Sparta fault which has been observed, for example, at the micrometer scale in surface coatings on the Magnola fault, because that scarp is comprised of pure carbonate (Carcaillet et al., 2008). It is likely that limestone fault scarps are generally composed of fault breccias (Agosta and Aydin, 2006; Carcaillet et al., 2008; Nuriel et al., 2012) and that where a fault intersects varying lithologies, chemical and mineralogical heterogeneities may occur in the fault breccia, as observed on the Sparta fault. Where they occur, these heterogeneities may control the spatial distribution of REY, independent of any spatial reorganization of REY attributable to subaerial weathering.

REY correlates with inferred clay abundances on the Sparta fault scarp (Fig. 9), rather than systematically with former soil profiles inferred from ^{36}Cl concentrations. A correlation of REY with Si and Al is indeed observed in the soils mantling the Sparta (R^2 = 0.71 and 0.45, respectively; Figs. 11c and S2b,c), Kaparelli (R^2 = 0.95 for Si; Figs. 1a and S4a), and Magnola fault hanging walls (R^2 = 0.98 for both Si and Al; Fig. S4b,c and electronic appendix to Manighetti et al., 2010). These correlations generally contrast with a weaker negative correlation between Y and pH (R^2 = 0.52) for the hanging wall soil on the Sparta Fault (Fig. 11c). We propose a causative relationship between the vertical distributions of REY and clay on the Sparta fault scarp. The presence of clay likely relates to fault breccia formation at considerable depths beneath the Earth's surface, rather than subaerial weathering processes. This reasoning is supported by the following observations:

(i) The Sparta fault scarp REY concentrations are equivalent to (Nuriel et al., 2012; Goodfellow et al., 2017) or higher than those measured elsewhere in platformal

https://doi.org/10.5194/egusphere-2023-1585
Preprint. Discussion started: 17 July 2023

limestone (Carcaillet et al., 2008; Mouslopoulou et al., 2011), but yttrium concentrations are lower than in the adjacent hanging wall soil (rare-earth elements were not measured; Tables S5, S7).

(ii) If REY exchange between the soil and fault scarp occurs according to the Carcaillet et al. (2008) model, fractionation of LREY and HREY elements is expected. For example, LREY might be preferentially mobilized (Takahashi et al., 2005; Carcaillet et al., 2008), leading to an enrichment of LREY relative to HREY in the fault scarp, where there are peaks in total REY. Conversely, LREY may be depleted relative to HREY where there are troughs in total REY. However, the proportion of LREY to HREY remains constant vertically along the Sparta fault scarp (Fig. 10).

(iii) There is no systematic decrease in total REY along the vertical scarp profile (Fig. 9), in contrast to declining concentrations with distance above the hanging wall on the Magnola fault (Carcaillet et al., 2008).

Whereas these observations discount subaerial weathering as the dominant mechanism for REY enrichment and depletion on the Sparta fault, there may be some weathering-induced exchange. This is evidenced by the peak in REY on the buried Sparta fault scarp correlating with the peak in soil acidity (Figs. 9, 11a, b), but which notably occurs in the subsurface, rather than at the soil surface. If, as we infer, the spatial patterning of REY, quartz, and clay (as indicated by Al) is inherited from depth, the observed wave-like signal (Figs. 6, 9) may reflect sorting and cementing of breccia around surface asperities on the fault plane. The resulting infilling of depressions with fault gauge may create a successively more polished and localized fault plane along which friction is lowered, thereby permitting larger slip (i.e., larger earthquakes) along the fault (Sagy and Brodsky, 2009). Whereas REY concentrations do not appear to be a reliable indicator of Holocene paleoseismicity along the Sparta fault, they may instead reveal processes that localize slip to a discrete fault plane.

https://doi.org/10.5194/egusphere-2023-1585
Preprint. Discussion started: 17 July 2023

6 Conclusion

In applying cosmogenic ^{36}Cl exposure-age dating and rare-earth elements and yttrium (REY) measurements to unravelling the paleoseismic history of the Sparta fault, Greece, we conclude the following: Modeling of ^{36}Cl concentrations along two vertical profiles on the Sparta Fault, closely adjacent to a ^{36}Cl concentration profile previously measured and interpreted by Benedetti et al. (2002), indicates that the scarp was likely exhumed over 5 earthquakes, including one at ~2.3 ± 0.2 kyr B.P., which correlates with the 464 B.C.E. event. Four earthquakes were clustered within a 1.5 kyr period that culminated with the 464 B.C.E. event. Cumulative uplift was as high as 2.8 mm yr^{-1} during that period, compared with ~0.6–0.9 mm a^{-1} over the preceding 2.7–4.4 kyr. Because earthquake activity may shift between faults in extensional settings, a large magnitude earthquake is not necessarily indicated as being overdue by the ~2.5 kyr that have elapsed since the 464 B.C.E. event. More generally, accurate identification of individual earthquakes is presently constrained by spatial variations in ^{36}Cl concentration profiles that reflect neither exposure duration nor imprints of former soil profiles. In cases where this is attributable to mineralogical variations, such as in the Sparta fault scarp, present chemical preparation techniques for AMS measurement of ^{36}Cl may insufficiently account for those variations.

The Sparta fault scarp is impure; it is composed of fault breccia, which contains quartz and clay-lined pores in addition to calcite. The vertical distribution of REY is highly correlated with the pore-clay and may indicate processes of fault evolution deep below the ground surface. The potential exchange of REY between the hanging wall colluvium and the adjacent footwall scarp is overwhelmed at this site by REY attached to the pore clays inherited from

https://doi.org/10.5194/egusphere-2023-1585
Preprint. Discussion started: 17 July 2023

depth. Because of this, Holocene earthquakes and their slip distances and magnitudes cannot be inferred for the Sparta fault from REY concentrations. This is probably true also for similar impure limestone fault scarps elsewhere.

Author contribution

AS conceived the study and AS, APS, MWC, RF, and BWG participated in fieldwork. RF conducted the analysis of scarp composition, made initial interpretations, and compiled an initial manuscript as a part of research studies at Stockholm University. BWG made additional analyses, including earthquake modelling, and led writing of this manuscript. GC led the laboratory preparation of samples for ^{36}Cl measurement, in which BWG also participated. GC calculated ^{36}Cl concentrations from the AMS data. All authors contributed to data interpretation and manuscript editing.

Competing interests

Arjen P. Stroeven is a member of the editorial board for Solid Earth.

Acknowledgements

We thank Mikael Amlert for his assistance with field safety and sampling, Giorgos Maneas, station manager of the Navarino Environmental Observatory (NEO), for his extensive assistance with field logistics, and our deceased friend, Dan Zetterberg, Department of Geological Sciences, Stockholm University, for his assistance with thin section preparations. This project was funded by the Stockholm University Research School for teachers focusing on Natural Hazards financed by the Swedish Research Council and by a grant from NEO. We gratefully acknowledge funding for fieldwork from the Swedish Society for Anthropology and Geography Andreé Fund to Fritzon.

References

Agosta, F. and Aydin, A.: Architecture and deformation mechanism of a basin bounding normal fault in Mesozoic platform carbonates, central Italy. Journal of Structural Geology, 28, 1445–1467, 2006.

Armijo, R., Lyon-Caen, H., and Papanastassiou, D.: A possible normal-fault rupture for the 464 BC Sparta earthquake. Nature, 351, 137–139, doi: 10.1038/351137a0, 1991.

Benedetti, L., Finkel, R., Papanastassiou, D., King, G., Armijo, R., Ryerson, F., Farber, D., and Flerit, F.: Post-glacial slip history of the Sparta fault (Greece) determined by ^{36}Cl cosmogenic dating: Evidence for non-periodic earthquakes. Geophysical Research Letters, 29, 1246, doi: 10.1029/2001GL014510, 2002.

Brandon, A: Clastic dykes in the Namurian shales of County Leitrim, Republic of Ireland. Geological Magazine, 109, 361–67, 1972.

Carcaillet, J., Manighetti, I., Chauvel, C., Schlagenhauf, A., and Nicole, J.-M.: Identifying past earthquakes on an active normal fault (Magnola, Italy) from the chemical analysis of its exhumed carbonate fault plane. Earth and Planetary Science Letters, 271, 145–158, doi: 10.1016/j.epsl.2008.03.059, 2008.

Cowie, P.A., Phillips, R.J., Roberts, G.P., McCaffrey, K., Zijerveld, L.J.J., Gregory, L.C., Faure Walker, J., Wedmore, L.N.J., Dunai, T.J., Binnie, S.A., Freeman, S.P.T.H., Wilcken, K., Shanks, R.P., Huismans, R.S., Papanikolaou, I., Michetti, A.M., and Wilkinson, M.: Orogen-scale uplift in the central Italian Apennines drives episodic behaviour of earthquake faults. Scientific Reports 7, 44858, 2017.

https://doi.org/10.5194/egusphere-2023-1585
Preprint. Discussion started: 17 July 2023

Darwin, C: Geological observations in the volcanic islands and parts of South America visited during the voyage of H.M.S. Beagle. London, 1840.

Dramis, F, and Blumetti, A.M.: Some considerations concerning seismic geomorphology and paleoseismology. Tectonophysics, 408, 177–191, 2005.

Evans, J.M, Stone, J.O.H., Fifield, L.K., and Cresswell, R.G.: Cosmogenic chlorine-36 production in K-feldspar. Nuclear Instruments and Methods in Physics Research B, 123, 334–340, 1997.

Fink, D., Vogt, S., and Hotchkis, M.: Cross-sections for ^{36}Cl from Ti at E_p = 35–150 MeV: Applications to in-situ exposure dating. Nuclear Instruments and Methods in Physics Research B, 172, 861–866, 2000.

Godey, S., Bossu, R., and Guilbert, J.: Improving the Mediterranean seismicity picture thanks to international collaborations. Physics and Chemistry of the Earth, Parts A/B/C 63, 3–11, doi:10.1016/j.pce.2013.04.012, 2013.

Goodfellow, B.W., Viola, G., Bingen, B., Nuriel, P., and Kylander-Clark, A.: Paleocene faulting in SE Sweden from U-Pb dating of slickenfiber calcite. Terra Nova 29, 321–328. https://doi.org/10.1111/ter.12280, 2017.

Gürpinar, A.: The importance of paleoseismology in seismic hazard studies for critical facilities. Tectonophysics, 408, 23–28, doi: 10.1016/j.tecto.2005.05.042, 2005.

Hickson, C.J. and Juras, S.J.: Sample contamination by grinding. Canadian Mineralogist 24, 585-589, 1986.

Hutchison, C.S.: Laboratory Handbook of Petrographic Techniques. Wiley-Interscience, New York, 527 pp, 1974.

Institute for Geology and Subsurface Research: Sparti Sheet, photogeological map of Greece, 1969.

Jolivet, L., Faccenna, C., Huet, B., Labrousse, L., Le Pourhiet, L., Lacombe, O., Lecomte, E., Burov, E., Denèle, Y., Brun, J.-P., Philippon, M., Paul, A., Salaün, G., Karabulut, H., Piromallo, C., Monié, P., Gueydan, F., Okay, A.I., Oberhänsli, R., Pourteau, A., Augier, R., Gadenne, L., and Driussi, O.: Aegean tectonics: Strain localisation, slab tearing and trench retreat. Tectonophysics, 597–598, 1–33, 2013.

Lifton, N.A., Bieber, J.W., Clem, J.M., Duldig, M.L., Evenson, P., Humble, J.E., and Pyle, R.: Addressing solar modulation and long-term uncertainties in scaling secondary cosmic rays for in situ cosmogenic nuclide applications. Earth and Planetary Science Letters, 239, 140–161, 2005.

Lifton, N.A., Sato, T., Dunai, T.J.: Scaling in situ cosmogenic nuclide production rates using analytical approximations to atmospheric cosmic-ray fluxes. Earth and Planetary Science Letters, 386, 149–160, 2014.

Lifton, N.A., Smart, D.F., Shea, M.A.: Scaling time-integrated in situ cosmogenic nuclide production rates using a continuous geomagnetic model. Earth and Planetary Science Letters, 268, 190–201, 2008.

Manighetti, I., Boucher, E., Chauvel, C., Schlagenhauf, A., Benedetti, L.: Rare earth elements record past earthquakes on exhumed limestone fault planes. Terra Nova, 22, 477–482, doi: 10.1111/j.1365-3121.2010.00969.x, 2010.

Marrero, S.M., Phillips, F.M., Caffee, M.W., Gosse, J.C.: CRONUS-Earth cosmogenic ^{36}Cl calibration. Quaternary Geochronology, 31, 199–219, 2016.

McCalpin, J.P.: Paleoseismology, Academic press, 613 pp., 2009.

McDonough, W.F., and Sun, S.-s.: The composition of the Earth. Chemical Geology, 120, 223–253, 1995.

Michetti, A.M., Audemard M., F.A. and Marco, S.: Future trends in paleoseismology: Integrated study of the seismic landscape as a vital tool in seismic hazard analyses Tectonophysics, 408, 3–21, 2005.

https://doi.org/10.5194/egusphere-2023-1585
Preprint. Discussion started: 17 July 2023

Mitchell, S.G., Matmon, A., Bierman, P.R., Enzel, Y., Caffee, M., and Rizzo, D.: Displacement history of a limestone normal fault scarp, northern Israel, from cosmogenic Cl-36. Journal of Geophysical Research-Solid Earth, 106, 4247–4264, doi: 10.1029/2000JB900373, 2001.
Moraetis, D., Mouslopoulou, V., and Pratikakis, A.: Sorption of the Rare Earth Elements and Yttrium (REE-Y) in calcite: the mechanism of a new effective tool in identifying paleoearthquakes on carbonate faults. Geophysical Research Abstracts, 17, EGU2015-3437, 2015.
Mouslopoulou, V., Moraetis, D., and Fassoulas, C.: Identifying past earthquakes on carbonate faults: Advances and limitations of the 'Rare Earth Element' method based on analysis of the Spili Fault, Crete, Greece. Earth and Planetary Science Letters, 309, 45–55, 2011.
Mozafari, N., Özkaymak, C., Sümer, Ö, Tikhomirov, D., Uzel, B., Yeşilyurt, S., Ivy-Ochs, S., Vockenhuber, C., Sözbilir, H., and Akçar, N.: Seismic history of western Anatolia during the last 16 kyr determined by cosmogenic ^{36}Cl dating. Swiss Journal of Geosciences 115, 5, https://doi.org/10.1186/s00015-022-00408-x, 2022.
Muhs, D.R., Budahn, J., Avila, A., Skipp, G., Freeman, J., Patterson, D.: The role of African dust in the formation of Quaternary soils on Mallorca, Spain and implications for the genesis of Red Mediterranean soils. Quaternary Science Reviews 29, 2518–2543, 2010.
Muzikar, P., Elmore, D., and Granger, D.E.: Accelerator mass spectrometry in geologic research. Geological Society of America Bulletin, 115, 643-654, doi: 10.1130/0016-7606(2003)115, 2003.
Nuriel, P., Rosenbaum, G., Zhao, J.-X., Feng, Y., Golding, S.D., Villemant, B., and Weinberger, R.: U-Th dating of striated fault planes. Geology, 40, 647–650, 2012.
Palumbo, L., Benedetti, L., Bourlès, D., Cinque, A., and Finkel, R.: Slip history of the Magnola fault (Apennines, Central Italy) from ^{36}Cl surface exposure dating: evidence for strong earthquakes over the Holocene. Earth and Planetary Science Letters, 225, 163–176, doi: 10.1016/j.epsl.2004.06.012, 2004.
Papanikolaou, I.D., Roberts, G.P., Deligiannakis, G., Sakellariou, A., and Vassilakis, E.: The Sparta Fault, Southern Greece: From segmentation and tectonic geomorphology to seismic hazard mapping and time dependent probabilities. Tectonophysics, 597–598, 85–105, 2013.
Pavlides, S. and Caputo, R.: Magnitude versus faults' surface parameters: quantitative relationships from the Aegean Region. Tectonophysics, 380, 159–188, 2004.
Pope, R.J. and Wilkinson, K.N.: Reconciling the roles of climate and tectonics in Late Quaternary fan development on the Spartan piedmont, Greece. In: A.M. Harvey, A.E. Mather, and M. Stokes, (Eds), Alluvial Fans: Geomorphology, Sedimentology, Dynamics. Geological Society, London, Special Publications, 251, 133–152. The Geological Society of London, 2005.
Röshoff, K. and Cosgrove, J.: Sedimentary dykes in the Oskarshamn-Västervik area. A study of the mechanism of formation. SKB Report R-02-37, 98 pp, 2002.
Roy, C.J.: Clastic dykes of the Pikes Peak region. Geological Society of America Bulletin, 57, 1226, 1946.
Sagy, A. and Brodsky, E.E.: Geometric and rheological asperities in an exposed fault zone. Journal of Geophysical Research, 114, B02301, doi: 10.1029/2008JB005701, 2009.
Schlagenhauf, A., Gaudemer, Y., Benedetti, L., Manighetti, I., Palumbo, L., Schimmelpfennig, I., Finkel, R., and Pou, K.: Using in situ Chlorine-36 cosmonuclide to recover past earthquake histories on limestone normal fault scarps: a reappraisal of methodology and interpretations. Geophysical Journal International, 182, 36–72, doi: 10.1111/j.1365-246X.2010.04622.x, 2010.

https://doi.org/10.5194/egusphere-2023-1585
Preprint. Discussion started: 17 July 2023

Sharma, P., Kubik, P.W., Fehn, U., Gove, H.E., Nishiizumi, K. and Elmore, D.: Development of Cl-36 Standards for AMS. Nuclear Instruments & Methods in Physics Research Section B-Beam Interactions with Materials and Atoms, 52, 410-415, doi: 10.1016/0168-583X(90)90447-3, 1990.

Sikora, F.J. and Moore, K.P. (Eds.): Soil Test Methods from the Southeastern United States. Southern Cooperative Series Bulletin, 419, 211 p., 2014.

Stone, J.O.: Air pressure and cosmogenic isotope production. Journal of Geophysical Research, 105, B10, 23753-23759, 2000.

Stone, J.O.: Terrestrial chlorine-36 production from spallation of iron. In: Abstract of 10th International Conference on Accelerator Mass Spectrometry, Berkeley, California, USA., 2005.

Stone, J.O., Allan, G.L., Fifield, L.K., and Cresswell, R.G.: Cosmogenic chlorine-36 from calcium spallation. Geochimica et Cosmochimica Acta, 60, 679-692, doi: 10.1016/0016-7037(95)00429-7, 1996.

Takahashi, Y., Chatellier, X., Hattori, K.H., Kato, K., and Fortin, D.: Adsorption of rare earth elements onto bacterial cell walls and its implication for REE sorption onto natural microbial mats. Chemical Geology, 219, 53–67, 2005.

Tesson, J., Pace, B., Benedetti, L., Visini, F., Delli Rocioli, M., Arnold, M., Aumaître, G., Bourlès, D.L., and Keddadouche, K.: Seismic slip history of the Pizzalto fault (central Apennines, Italy) using in situ-produced ^{36}Cl cosmic ray exposure dating and rare earth element concentrations. Journal of Geophysical Research Solid Earth, 121, 1983–2003, doi:10.1002/2015JB012565, 2016.

Woodcock, N.H. and Mort, K.: Classification of fault breccias and related fault rocks. Geological Magazine, 145, 435–440, doi: 10.1017/S0016756808004883, 2008.

Zreda, M. and Noller, J.: Ages of prehistoric earthquakes revealed by cosmogenic chlorine-36 in a bedrock fault scarp at Hebgen Lake. Science, 282, 1097–1099, 1998.

https://doi.org/10.5194/egusphere-2023-1585
Preprint. Discussion started: 17 July 2023

Table 1: Parameters used to give best fits of modelled profiles to measured ^{36}Cl concentration profiles, following Schlagenhauf et al. (2010).

Profile	α (°)	β (°)	γ (°)	Scarp (cm)	ρ_{rock} (g cm^{-3})	$\rho_{colluvium}$ (g cm^{-3})	^{36}Cl P_o (at. g^{-1} yr^{-1})	ε (mm yr^{-1})	Pre (yr)	Age (kyr B.P.)	Slip (cm)	RMSw	AICc	χ^2_{red}
Fig. 3a	42	61	20	730	2.65	1.95	59.4	0.02	10 300	5.98 ± 0.4, 3.8 ± 0.3, 3.2 ± 0.3, 2.8 ± 0.2, 2.3 ± 0.2	140, 120, 130, 120, 140	10	859	3
Fig. 3b	49	61	20	730	2.65	2.01	59.4	0.02	3 900	2.5 ± 0.2, 2.3 ± 0.2	60, 140	5	406	2
Fig. 3c	42	61	20	742	2.65	1.95	59.4	0.02	12 000	8.6 ± 0.6, 5.8 ± 0.4, 3.8 ± 0.3, 3.2 ± 0.3, 2.5 ± 0.3	140, 120, 130, 120, 140	19	1338	7
Fig. 3d	42	61	20	730	2.65	1.95	59.4	0.02	10 300	5.9 ± 0.4, 3.0 ± 0.3, 2.8 ± 0.2, 1.9 ± 0.2	240, 140, 180, 80	12	875	5

α is hanging wall colluvial surface dip angle; β is scarp dip angle; γ is the dip angle of the hillslope above the fault scarp; ε is scarp erosion rate; Pre is pre-exposure; Age is inferred earthquake age(s) with 0 inserted to model scarp samples from below the surface of the hanging wall colluvium; Slip is the inferred displacement for each earthquake. On each profile, the oldest age and associated displacement, shown in grey, are fitted to the top of the vertical sample transect rather than fitted to a step in ^{36}Cl concentration; RMSw is weighted root mean square; AICc is Akaike Information Criterion; χ^2_{red} is reduced Chi-square. Model best fits for each data set are shown in black. The ^{36}Cl production rate of 59.4 ± 4.3 at g^{-1} yr^{-1} is taken from Lifton et al. (2005).

https://doi.org/10.5194/egusphere-2023-1585
Preprint. Discussion started: 17 July 2023

889 **Figures**

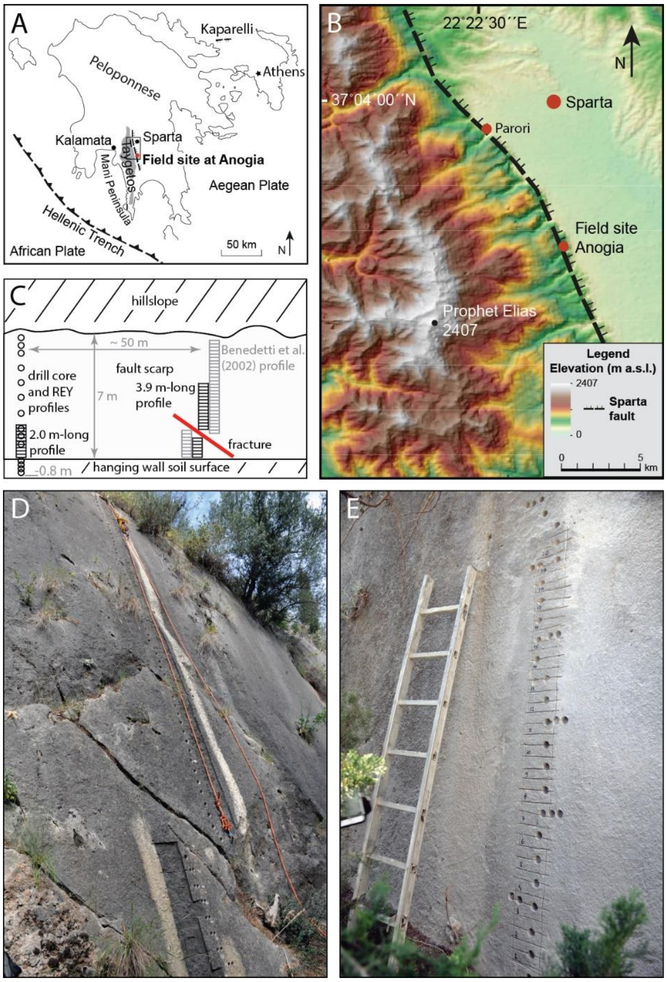

890

891 **Fig. 1:** Study site. A. The study site location in Peloponnese, Greece. Key tectonic features
892 are shown. Box indicates location of panel B. B. The location of the Sparta fault, separating
893 the Taygetos Mountains from the Sparta basin. The location of the Anogia field site used both
894 in this study and in Benedetti et al. (2002) is shown. Benedetti et al. (2002) located a second
895 sampling transect at Parori (also shown). The digital elevation model has a 24 m resolution
896 and is derived from ASTER GDEM (GDEM2), which is a product of NASA and METI
897 (Japan). C. Schematic diagram of the Sparta fault scarp at Anogia, showing the locations of
898 our vertical ^{36}Cl and REY sampling transects, and the ^{36}Cl sampling transect of Benedetti et
899 al. (2002). D. Photograph showing the location of our 3.9 m-long profile, prior to sampling.
900 The existing sample scar is from Benedetti et al. (2002). E. Photograph showing the location
901 of our REY and drill core profiles, after sampling, and our 2.0 m long profile, before
902 sampling.

https://doi.org/10.5194/egusphere-2023-1585
Preprint. Discussion started: 17 July 2023

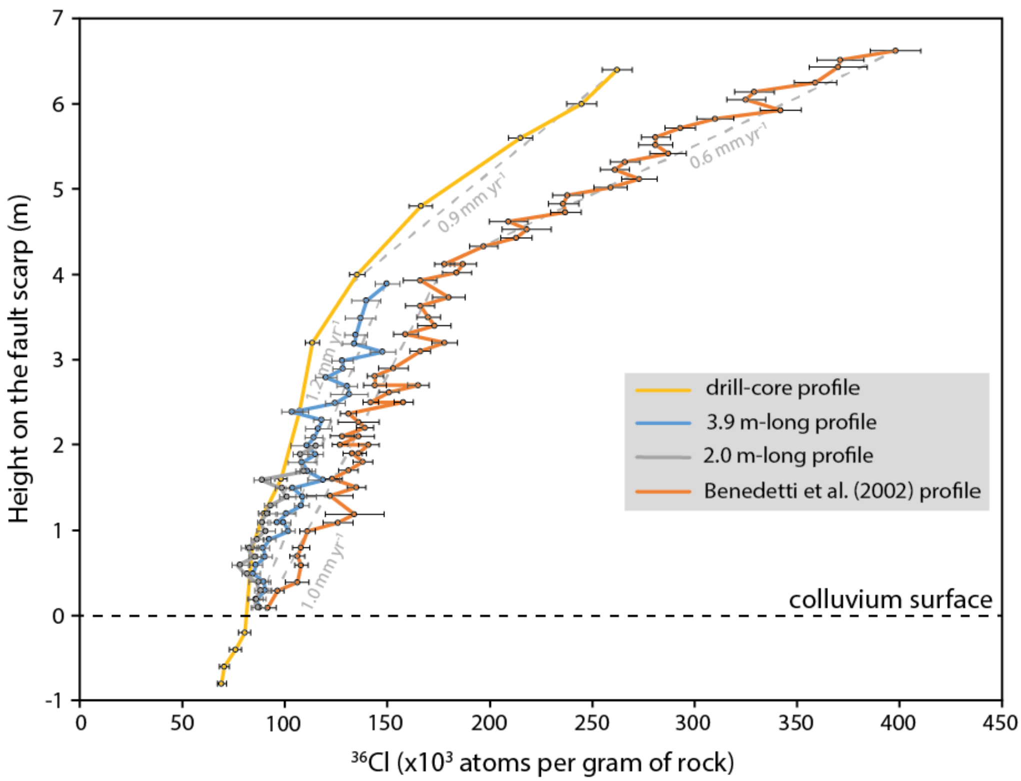

Fig. 2: Sparta fault ^{36}Cl concentration profiles. Error bars indicate 1σ measurement uncertainties. Time-averaged uplift rates inferred from profile gradients are shown in grey. For the lower, more recently exposed, parts of the scarp surface, uplift rates are calculated for time starting from the present day. If uplift rates are alternatively calculated as occurring prior to the subaerial exposure of the lowermost samples by the most recent earthquake, cumulative uplift rates increase to 2.8 mm yr^{-1} and 1.8 mm yr^{-1} for the lower parts of the 3.9 m-long and Benedetti et al. (2002) profiles, respectively.

https://doi.org/10.5194/egusphere-2023-1585
Preprint. Discussion started: 17 July 2023

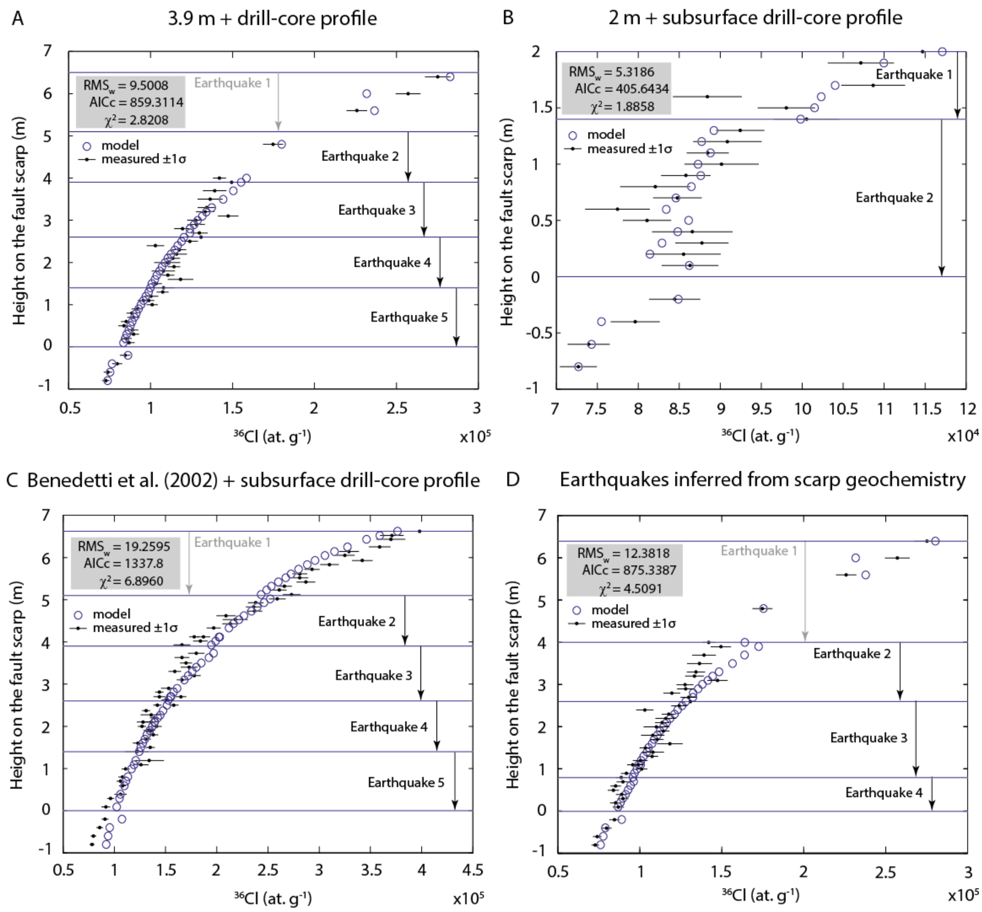

Fig. 3: Best fits of profiles modelled according to Schlagenhauf et al. (2010) to measured Sparta fault ^{36}Cl concentration profiles. Down-arrows indicate the section of scarp exhumed during each earthquake. Best fits of modelled profiles to measured data are indicated by lowest attainable values for each of RMS$_w$, χ^2_{red}, and AICc. A. Anogia 3.9 m profile plus drill core profile data above 3.9 m and below the present hanging wall colluvium surface. B. Anogia 2.0 m profile plus drill core profile data from below the present hanging wall colluvium surface. C. Benedetti et al. (2002) data, remodeled using the same parameters as for panel A . The modelled profile is smooth because scarp composition is based on a mean value taken from our data. Our drill core subsurface samples were also used to help remodel the Benedetti et al. (2002) data, which required adding 13% on to their measured concentrations. D. Same profile as in A but with earthquakes inferred from the fault scarp geochemistry.

https://doi.org/10.5194/egusphere-2023-1585
Preprint. Discussion started: 17 July 2023

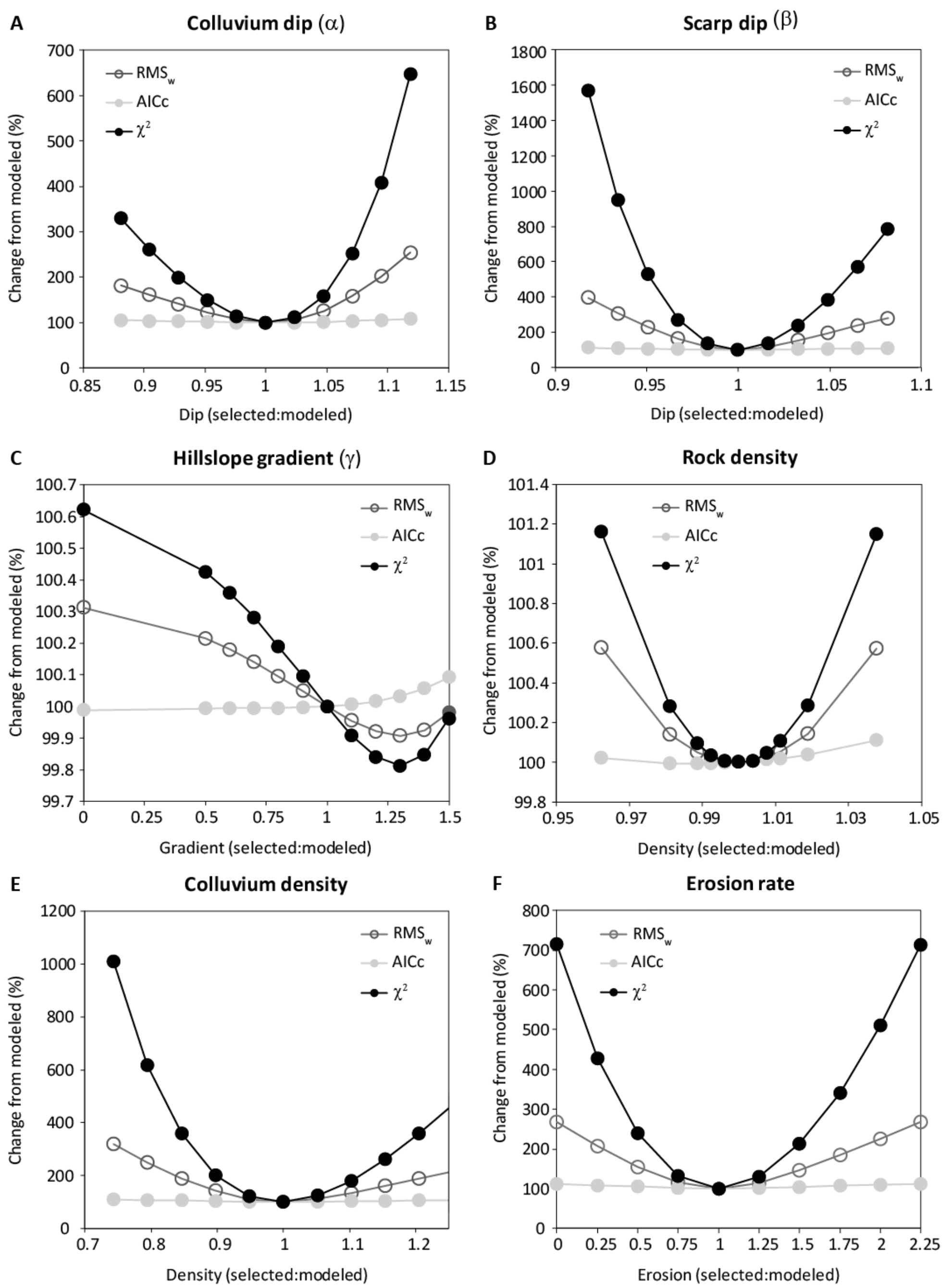

Fig. 4: Sensitivity of fits of profiles modelled according to Schlagenhauf et al. (2010) to measured Sparta fault ^{36}Cl concentration profiles, according to input parameters. A. Colluvial wedge dip B. Scarp dip C. Slope angle above the scarp. D. Scarp rock density E. Colluvium density F. Scarp erosion rate.

https://doi.org/10.5194/egusphere-2023-1585
Preprint. Discussion started: 17 July 2023

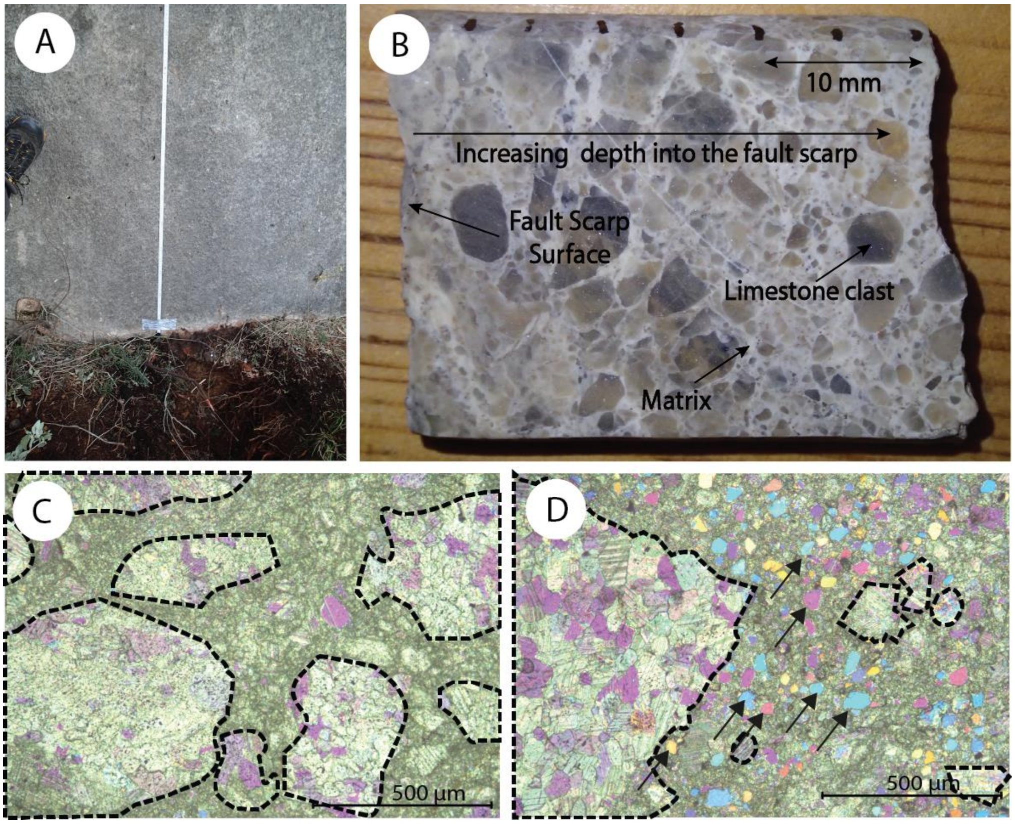

Fig. 5: The heterogeneous fault breccia that comprises the Sparta fault scarp surface. A. The Sparta fault scarp surface appears smooth and homogenous, as illustrated by this photograph of the scarp base at Anogia (upper half of the dug trench in the foreground). B. Fault breccia is revealed in a cut drill core, where clasts of host limestone are cemented in a fine matrix. C. A photomicrograph shows limestone clasts (dotted outlines) comprising about 60% of the thin section area. D. A photomicrograph shows fine matrix comprising about 60% of the thin section area. Arrows indicate quartz.

https://doi.org/10.5194/egusphere-2023-1585
Preprint. Discussion started: 17 July 2023

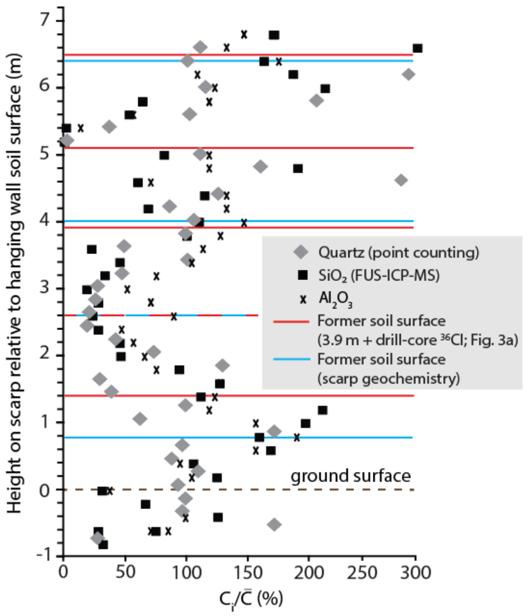

Fig. 6: Concentrations of Al_2O_3 and SiO_2, and quartz abundances from point counting, along a vertical profile, Sparta fault scarp, Anogia. The concentration of each element (C_i) is normalized to its mean concentration through the profile ($C_i/\bar{C}$). The locations of former soil surface horizons inferred from ^{36}Cl concentrations and from the scarp geochemistry are shown for reference.

https://doi.org/10.5194/egusphere-2023-1585
Preprint. Discussion started: 17 July 2023

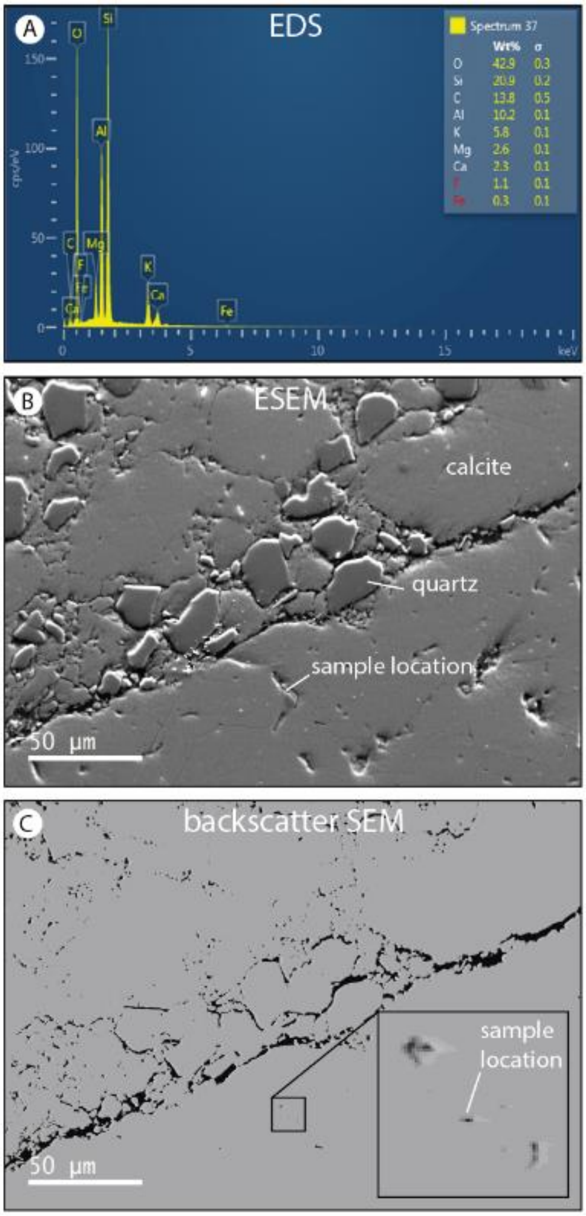

Fig. 7: Energy-dispersive X-ray spectroscope (EDS) elemental abundances, and environmental scanning electron microscope (ESEM) and backscatter SEM imagery of a thin section of fault breccia comprising the Sparta fault scarp surface at 1.1 m above the hanging wall. (A). Element abundances in a pore, the location of which is shown in panels B and C. Si, Al, and K are abundant relative to Ca, which indicates that clay, e.g., illite, is lining the pore. (B) Quartz is an abundant constituent of the thin section matrix. (C) Porosity, shown in black; note its spatial association with quartz. The location of the sample used in panel A is in a small pore, shown in the inset.

https://doi.org/10.5194/egusphere-2023-1585
Preprint. Discussion started: 17 July 2023

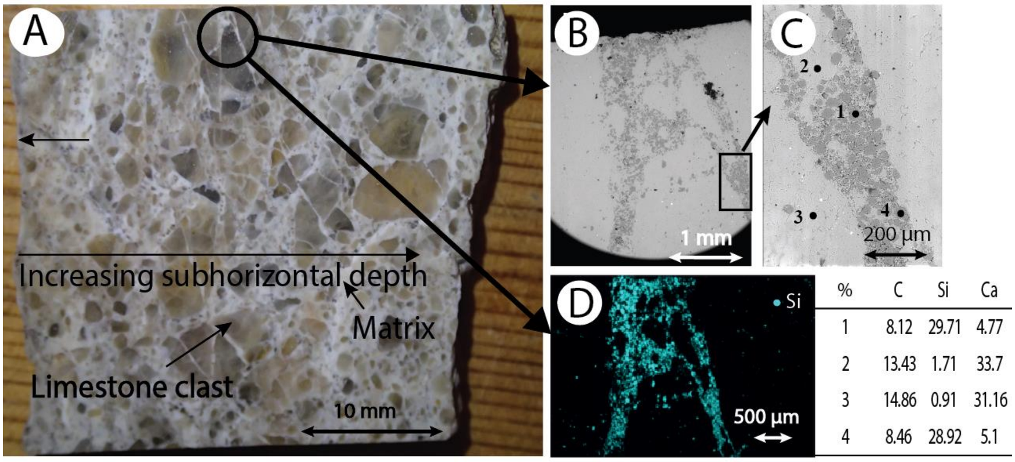

%	C	Si	Ca
1	8.12	29.71	4.77
2	13.43	1.71	33.7
3	14.86	0.91	31.16
4	8.46	28.92	5.1

Fig. 8: Concentrations of Si in the Sparta fault breccia, 1.1 m above the scarp base at Anogia. A. A cut drill core from the Sparta fault scarp at Anogia showing limestone clasts cemented in fine matrix. The circled fine matrix is examined under high resolution in panels B to D. B. An ESEM image showing the sample location for spot elemental analysis (rectangle). C. Sample points for elemental analysis using EDS, with values shown in the table. D. The abundance of Si in the fine matrix illustrated in magenta for the circled part of the thin section shown in panel A.

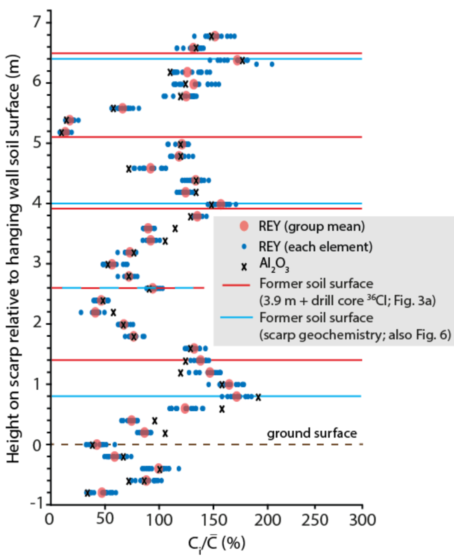

Fig. 9: Concentrations of rare-earth elements and yttrium (REY) along a vertical profile on the Sparta fault at Anogia. Mean values for all REY elements at each sample point are shown in red dots, whereas individual REY elements are shown in blue dots. The concentration of each element (C_i) is normalized to its mean concentration through the profile ($C_i/\overline{C}$).

https://doi.org/10.5194/egusphere-2023-1585
Preprint. Discussion started: 17 July 2023

Concentrations of Al_2O_3 and former soil surface horizons inferred from ^{36}Cl concentrations profiles and geochemical data, are shown for reference.

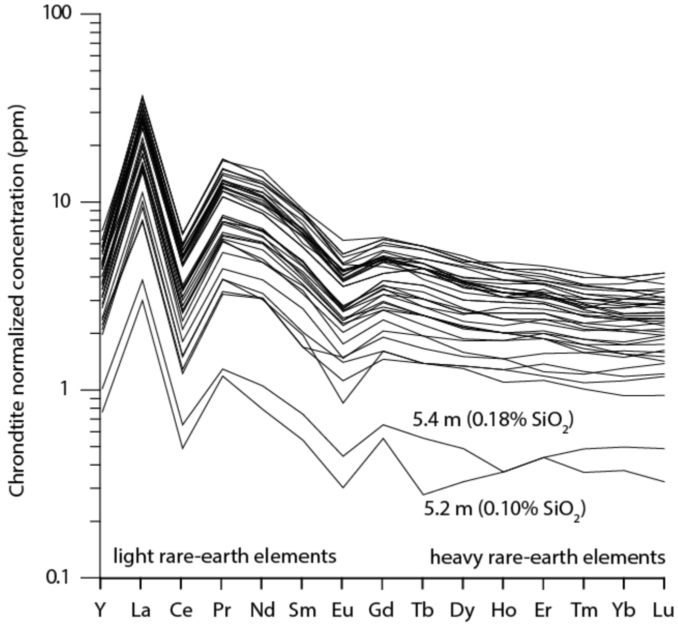

Fig. 10: Concentrations of rare-earth elements and yttrium (REY) normalized to chondrite composition (McDonough and Sun, 1995) for the Sparta Fault scarp at Anogia. Each line shows a measured location on the scarp surface. The two low REY outliers at 5.2 m and 5.4 m also have exceptionally low SiO_2.

https://doi.org/10.5194/egusphere-2023-1585
Preprint. Discussion started: 17 July 2023

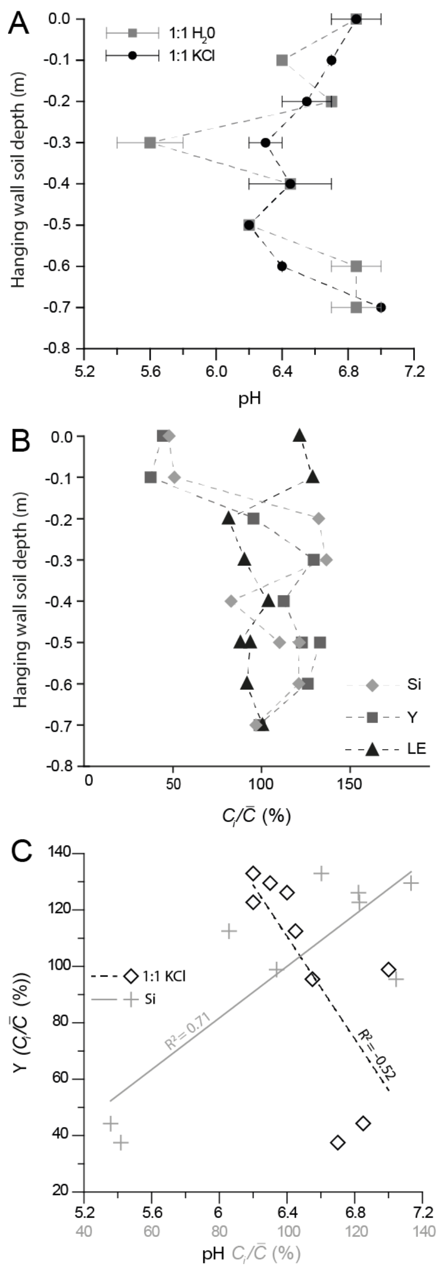

Fig. 11: Hanging wall soil chemistry, adjacent to the Sparta fault scarp at Anogia. A. Soil pH along a vertical profile measured from soil mixed with distilled H_2O and 1M KCl. Uncertainty ranges show the ≤ 0.5 resolution of the indicator strips. B. Concentrations of Si, Y, and elements too light to be measured using handheld XRF (LE, including C) along the vertical soil profile. Each element has been normalized through division by its mean concentration through the soil. C. Y concentrations plotted against pH (measured from 1:1 KCl) and Si concentration at each measured depth interval beneath the soil surface.